



Rice, K., Batul, K., Whiteside, J., Kelso, J., Papinski, M., Schmidt, E., Pratasouskaya, A., Wang, D., Sullivan, R., Bartlett, C., Weadge, J., Van der Kamp, M., Moreno-Hagelsieb, G., Suits, M., & Horsman, G. (2019). The predominance of nucleotidyl activation in bacterial phosphonate biosynthesis. *Nature Communications*, 10(1), [3698 (2019)]. <https://doi.org/10.1038/s41467-019-11627-6>

Publisher's PDF, also known as Version of record

License (if available):
CC BY

Link to published version (if available):
[10.1038/s41467-019-11627-6](https://doi.org/10.1038/s41467-019-11627-6)

[Link to publication record in Explore Bristol Research](#)
PDF-document

This is the final published version of the article (version of record). It first appeared online via Springer Nature at <https://www.nature.com/articles/s41467-019-11627-6#Sec30>. Please refer to any applicable terms of use of the publisher.

University of Bristol - Explore Bristol Research

General rights















This document is made available in accordance with publisher policies. Please cite only the published version using the reference above. Full terms of use are available:
<http://www.bristol.ac.uk/red/research-policy/pure/user-guides/ebr-terms/>

ARTICLE

<https://doi.org/10.1038/s41467-019-11627-6>

OPEN

The predominance of nucleotidyl activation in bacterial phosphonate biosynthesis

Kyle Rice ¹, Kissa Batul¹, Jacqueline Whiteside ¹, Jayne Kelso ¹, Monica Papinski ^{1,2}, Edward Schmidt ¹, Alena Pratasouskaya ¹, Dacheng Wang ¹, Rebecca Sullivan ¹, Christopher Bartlett ², Joel T. Weadge ², Marc W. Van der Kamp ³, Gabriel Moreno-Hagelsieb ², Michael D. Suits ¹ & Geoff P. Horsman ¹

Phosphonates are rare and unusually bioactive natural products. However, most bacterial phosphonate biosynthetic capacity is dedicated to tailoring cell surfaces with molecules like 2-aminoethylphosphonate (AEP). Although phosphoenolpyruvate mutase (Ppm)-catalyzed installation of C-P bonds is known, subsequent phosphonyl tailoring (Pnt) pathway steps remain enigmatic. Here we identify nucleotidyltransferases in over two-thirds of phosphonate biosynthetic gene clusters, including direct fusions to ~60% of Ppm enzymes. We characterize two putative phosphonyl tailoring cytidyltransferases (PntCs) that prefer AEP over phosphocholine (P-Cho) – a similar substrate used by the related enzyme LicC, which is a virulence factor in *Streptococcus pneumoniae*. PntC structural analyses reveal steric discrimination against phosphocholine. These findings highlight nucleotidyl activation as a predominant chemical logic in phosphonate biosynthesis and set the stage for probing diverse phosphonyl tailoring pathways.

¹Department of Chemistry & Biochemistry, Wilfrid Laurier University, Waterloo, ON N2L 3C5, Canada. ²Department of Biology, Wilfrid Laurier University, Waterloo, ON N2L 3C5, Canada. ³School of Biochemistry, University of Bristol, Bristol BS8 1TD, UK. Correspondence and requests for materials should be addressed to G.P.H. (email: ghorsman@wlu.ca)

With stability and bioactivity imparted by a characteristic carbon–phosphorus bond, phosphonates are unusual and relatively unexplored biological molecules. Since the discovery of 2-aminoethylphosphonate (AEP) in nature six decades ago¹, phosphonates and phosphinates have gained recognition as a small but commercially successful class of natural products exemplified by the antibiotic fosfomycin and the herbicide phosphinothricin (Fig. 1a)^{2,3}. Although exploration of these molecules and their biosynthesis is still in its infancy, bioinformatic analyses have revealed widespread genetic capacity to produce chemically diverse phosphonates^{4–6}. For example, ~5% of sampled microbes encode phosphoenolpyruvate mutase (Ppm)⁴, which catalyzes rearrangement of phosphoenolpyruvate (PEP) to the C–P bond-containing product phosphonopyruvate (PnPy) (Fig. 1b)⁷. Despite this predicted ubiquity, natural product classes like polyketides and nonribosomal peptides have been far more intensively investigated, and the relative dearth of characterized phosphonates partly reflects technical challenges associated with high polarity and lack of chromophores⁸. However, the few phosphonate biosynthetic gene clusters that have been characterized have revealed unusual enzymes catalyzing unprecedented chemical transformations⁹. These findings highlight the gap between current biosynthetic knowledge and future discovery potential, and motivate continued investigation of biological phosphonates.

Even more overlooked than freely diffusible small molecule phosphonates are those that modify, or tailor, cell surfaces. Comprehensive bioinformatic analysis of microbial *ppm* gene distribution predicted that most putative phosphonate biosynthetic gene clusters encode cell wall phosphonoglycans and phosphonolipids⁴. Although a handful of phosphorylated glycans and lipids have been structurally identified—such as the AEP-modified capsular polysaccharide from *Bacteroides fragilis*¹⁰ (Fig. 1c)—almost nothing is known about their biosynthesis or biological roles. Modulating biological function by adding or removing small molecules on cell surface materials has long been recognized as a key mechanism of bacterial adaptation and virulence. Common cell surface modifications include the addition of acetyl¹¹, pyruvyl¹², phosphoethanolamine^{13,14}, and phosphocholine (P-Cho)^{15–17} groups to lipids and glycans. Indeed, P-Cho is a virulence factor encoded by the Lic pathway in pathogens, such as *Streptococcus pneumoniae*^{15,18}, and *lic* gene disruption impedes P-Cho decoration of teichoic acids and attenuates *S. pneumoniae* virulence^{19–21}. Understanding the biosynthetic logic of these modifications

therefore represents an important goal with therapeutic implications, as phosphonates may similarly modulate virulence.

To address the gap between bioinformatic prediction and biosynthetic knowledge, we are characterizing several biosynthetic gene clusters predicted to encode cell wall phosphonoglycans or phosphonolipids. For instance, guided by the presence of *ppm* genes, we previously identified gene expression and/or phosphonate production from anaerobic bacteria *Atopobium rimae*, *Treponema denticola*, and *Olsenella uli*²², each of which have been associated with disease of the human oral cavity^{23–25}. Commonly associated with *ppm* and found in these gene clusters are *ppd* and *aep*, which respectively, encode PnPy decarboxylase (Ppd) and AEP transaminase (AEPT) to generate AEP (Fig. 1b)^{26,27}. Unfortunately, additional genes commonly found in predicted phosphonyl tailoring gene clusters have not been described, and the biosynthetic steps leading to phosphonyl modifications remain unknown (Fig. 1). Herein we reveal widespread occurrence of nucleotidyltransferase-encoding genes in phosphonate biosynthesis and characterize two representative enzymes as phosphonate-specific cytidyltransferases from the Gram-positive actinobacterium *A. rimae* and the Gram-negative spirochete *T. denticola*. These enzymes efficiently activate AEP, presumably for subsequent capture by carbohydrate or lipid nucleophiles. We propose the phosphonyl tailoring (*pnt*) nomenclature for these gene clusters, and specifically use PntC for AEP cytidyltransferase based on its sequence and biosynthetic similarity to LicC of the P-Cho tailoring (Lic) pathway. Indeed, in contrast to PntC, LicC from *S. pneumoniae* (Spn-LicC) strongly prefers P-Cho over AEP as a substrate for cytidyl activation. Structure determination of PntC from *T. denticola* (Tde-PntC) and molecular dynamics analyses indicate that PntC selectivity for the smaller AEP substrate is primarily driven by active site steric constraints. Overall, identifying this remarkably widespread family of phosphonate-specific PntC cytidyltransferases sets the stage for deciphering the biosynthetic roles of CMP-phosphonate conjugates and the biological consequences of this underexplored cell surface chemistry.

Results

Nucleotidyltransferases are enriched in phosphonate biosynthesis. To identify enzymes commonly associated with Ppm, we assessed Ppm protein sequences for the presence of fused domains. Precedent for active Ppm fusion proteins was

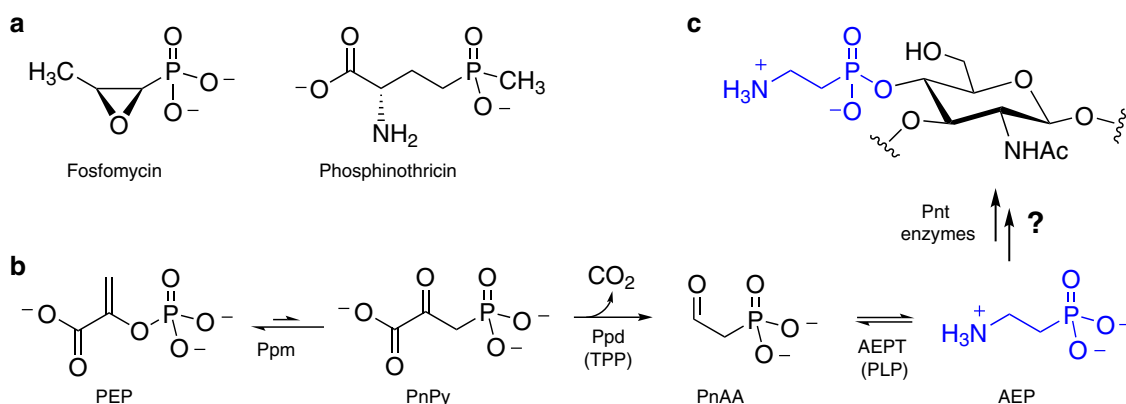


Fig. 1 Phosphonates in nature. **a** Small molecule bioactive natural products fosfomycin and phosphinothricin. **b** Biosynthesis of the common phosphonate AEP from phosphoenolpyruvate (PEP) via the intermediacy of phosphonopyruvate (PnPy) and phosphonoacetaldehyde (PnAA). Cofactors in parentheses are thiamine pyrophosphate (TPP) and pyridoxal 5'-phosphate (PLP). Unknown phosphonyl tailoring (Pnt) biosynthetic steps lead from AEP to **c**, cell surface phosphonoglycans like that isolated from *Bacteroides fragilis*

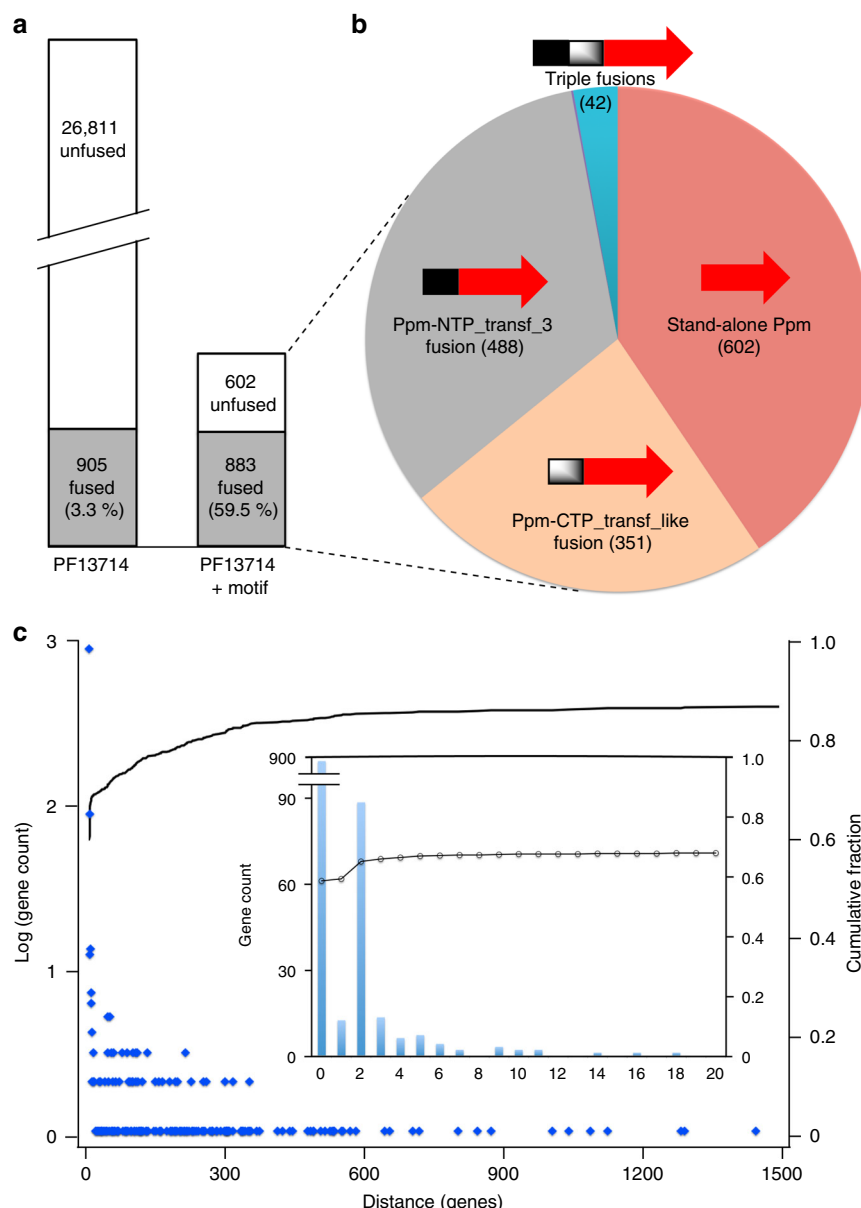


Fig. 2 Genomic relationships between *ppm* and nucleotidyltransferase-encoding genes. **a** Left: 27,716 non-redundant Ppm protein sequences were identified in NCBI's refSeq prokaryotic genome database that matched the PF13714 HMM, of which 905 were fused to other domains. Right: After filtering for the presence of the characteristic Ppm motif (EDKXXXXXNS), 26,231 presumed non-Ppm sequences were removed. Only 22 of these removed sequences were fused to other domains. **b** Summary of the remaining 1485 predicted Ppm proteins and inventory of fusion status: Ppm alone (red, 40.5%); PF12804, MobA-like NTP transferase (NTP_transf_3; gray, 32.9%); PF01467, Cytidyltransferase-like (CTP_transf_like; orange, 23.6%); not visible are two genes matching PF02775 and PF02776 (both TPP-binding domains), which corresponds to 0.1% of non-redundant Ppm proteins. The blue slice represents 42 triple fusion proteins (2.8% of all Ppm proteins) with Ppm fused to both PF12804 and PF01467. **c** Distribution of genomic distances (in genes) between *ppm* and the nearest of either PF12804 or PF01467. Blue dots represent logarithm of the number of genes counted for each distance (corresponding to left y-axis), and the line represents the cumulative fraction of genomic distances (right y-axis); 59.3% of nearest nucleotidyltransferase genes (those closest to *ppm*) are fused to *ppm* (distance = 0), and only single counts occur at distances greater than ~350 genes. *Inset*: Number of genes for each distance up to 20, illustrating that two-thirds of nucleotidyltransferase genes are within -5 genes of *ppm*

recently established in the *Streptomyces wedmorensis* fosfomycin biosynthetic pathway. The Ppm enzyme Fom1 possesses an *N*-terminally fused cytidyltransferase (CyTase) domain catalyzing cytidyltransfer from CTP to hydroxyethylphosphonate (HEP) to generate CMP-HEP²⁸. Inspired by this example of a biosynthetically relevant Ppm-fused domain, we generated a Ppm fusion inventory (Fig. 2). From the NCBI refSeq database containing 113,086 genomes we identified 146,399 proteins in 72,350 genomes matching the hidden Markov model (HMM) for the Ppm/isocitrate lyase Pfam family (PF13714). After filtering out

identical sequences we were left with 27,716 non-redundant protein sequences matching PF13714, of which only 905 (3.3%) were fused to another Pfam domain (Fig. 2a). Of the 27,716 total sequences, only 1485 possessed the Ppm-specific EDKXXXXXNS motif⁴. Surprisingly, almost all fusions (883 out of 905) possessed this motif, indicating that the majority of Ppm enzymes (59.5%) are fused to other domains (Fig. 2a) in what represents an unusual and potentially distinguishing feature of the Ppm enzyme family. Indeed, only 40.5% of Ppm enzymes were 'stand-alone' proteins not fused to any other domain, and most Ppm enzymes

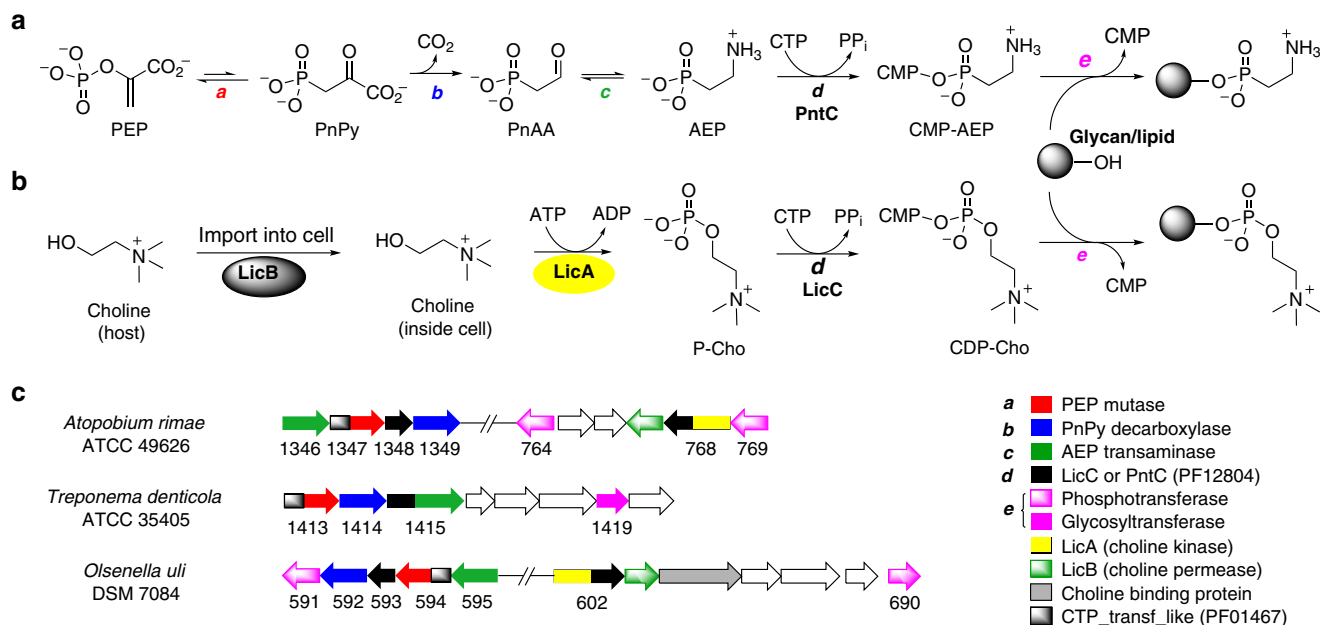


Fig. 3 Bacterial cell surface modifications employing cytidyl activation. **a** Proposed phosphonyl tailoring (Pnt) pathway logic based on its similarity to **b** the lipopolysaccharide core (Lic) pathway. **c** Putative gene clusters for three oral anaerobes under study, highlighting relevant genes for phosphocholine (P-Cho) and phosphonate tailoring. Black-colored genes are proposed to encode phosphonate-tailoring cytidyltransferases (PntCs) when located near *ppm* genes (red), and P-Cho cytidyltransferases (LicC) when located near other *lic* genes (e.g. those encoding LicA shown in yellow). For clarity, annotations for uncolored genes are not included

were fused to the MobA-like NTP transferase domain (PF12804, 33.0%), to the cytidyltransferase-like domain (PF01467, 23.6%), or both (2.9%, Fig. 2b). PF12804 is exemplified by Spn-LicC²⁹, and PF01467 by the Fom1 CyTase²⁸.

This predominance of nucleotidyltransferase domains fused to Ppm enzymes was unexpected and supports a co-evolutionary trajectory of the two catalytic activities. In bacteria, co-evolution of functionally related genes is generally observed as co-localization, or clustering, on the chromosome³⁰. A compilation of calculated distances, in number of genes, between *ppm* and the nearest gene encoding either PF12804 or PF01467 clearly illustrated a tendency for these genes to be in close proximity (Fig. 2c). For instance, 59.3% of all nearest nucleotidyltransferases were fused to *ppm* (distance = 0 genes). The next most frequent distance was two genes away, and about two-thirds (67.7%) of nucleotidyltransferases were within five genes of *ppm* (Fig. 2c inset). Note that these calculations identify only the nearest nucleotidyltransferase in a given gene cluster and therefore do not account for gene clusters possessing more than one nucleotidyltransferase. For example, the gene clusters in Fig. 3c possess nucleotidyltransferases that are both *ppm*-fused as well as one or two genes away. In these cases only the nearest nucleotidyltransferase would be tabulated, which for all three would be the fused domain at a distance of zero. In summary, this proximity bias indicates a functional relationship between Ppm and nucleotidyltransferases, and strongly implies an important role for the latter in phosphonate biosynthesis.

Interestingly, many *ppm*-associated nucleotidyltransferases are annotated as LicC-like cytidyltransferases, which provides an important clue regarding possible biosynthetic function. The *lic* (lipopolysaccharide core) operon catalyzes choline import, phosphorylation and attachment of P-Cho to a glycan substrate destined for the cell wall^{18,31}. Mirroring the chemical logic of the eukaryotic Kennedy pathway, a LicC cytidyltransferase catalyzes formation of CDP-choline from CTP and P-Cho (Fig. 3b). LicC from *S. pneumoniae* (Spn-LicC) has been structurally and biochemically characterized^{29,32,33}, and gene disruption attenuated virulence in a

mouse model²¹. Overall, the similarities between P-Cho and AEP and genomic proximity of *ppm* and *licC*-like genes suggested that phosphonates may be activated as CMP-conjugates in a manner analogous to P-Cho activation by LicC (Fig. 3a).

PntC enzymes preferentially activate AEP. Intrigued by the genomic proximity of *ppm* and *licC*-like cytidyltransferases, we sought to characterize the putative phosphonate-specific nucleotidyltransferases Oul593, Ari1348 and Tde1415. We observed transcription of *oul593* and *ari1348* in pure cultures (Supplementary Fig. 1), and previously reported chemical shifts consistent with phosphonates via solid-state ³¹P NMR analysis of *T. denticola* and *O. uli* whole cells²². Furthermore, each genomic neighborhood encodes AEP production and biosynthetic machinery associated with cell wall glycans, such as LicD-like phosphotransferases or glycosyltransferases (Fig. 3c). In fact, both *A. rimae* and *O. uli* possess *lic* genes relatively nearby on the chromosome. The Ppm protein sequences also phylogenetically cluster into phosphonoglycan/lipid clades^{4,22}, which further suggests that these phosphonates are directed to the cell surface. To evaluate the substrate preference of putative phosphonate nucleotidyltransferases relative to Spn-LicC, we expressed and purified Ari1348, Tde1415, and Spn-LicC, but Oul593 was insoluble (Supplementary Fig. 2). Dynamic light scattering (DLS) analysis indicated monomeric quaternary structures for Spn-LicC and Ari1348 (Supplementary Fig. 3), as previously observed for Spn-LicC³³. In contrast, Tde1415 has a predicted monomeric molecular weight of ~70 kDa with DLS data indicating a dimer of ~146 kDa.

Cytidyltransferase activity detected using an HPLC assay revealed time-dependent formation of CDP-choline (CDP-Cho) and CMP-AEP by Spn-LicC and Ari1348, respectively (Fig. 4a). CDP-Cho was verified by comparison to commercially sourced authentic standard and high-resolution mass spectrometry (expected mass, 488.1073; observed, 488.1071). CMP-AEP was identified based on high-resolution mass spectrometry and

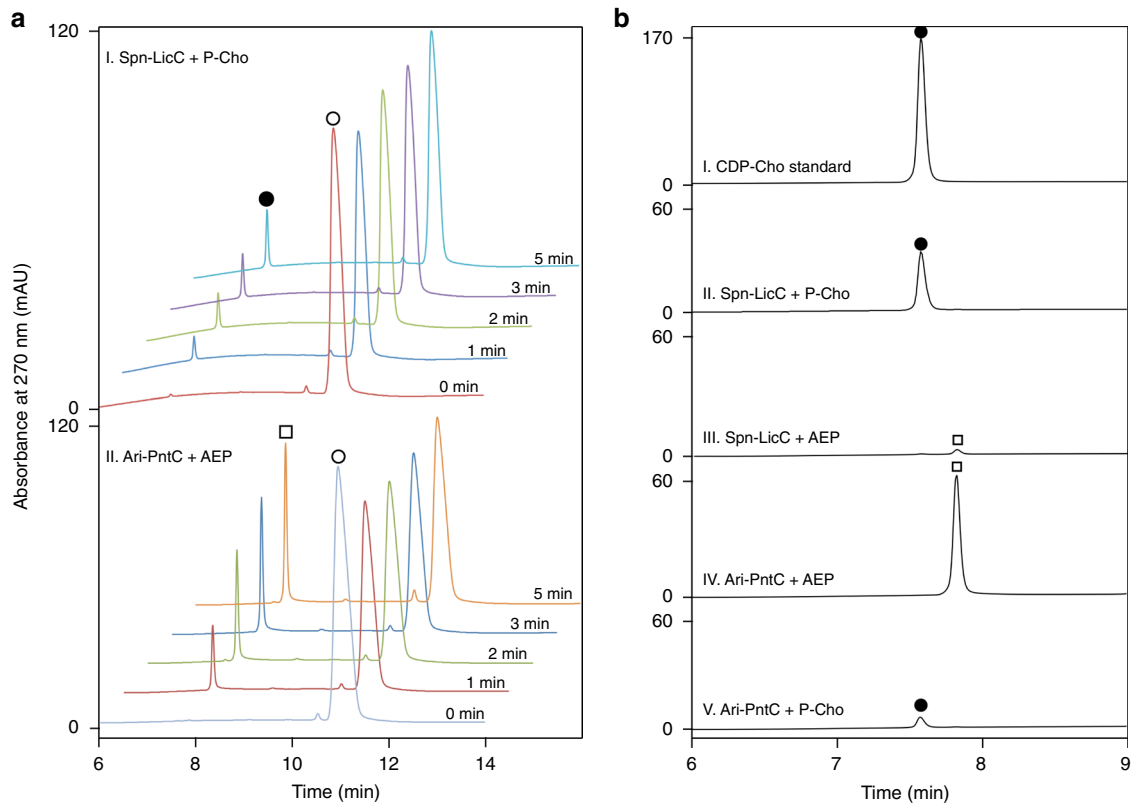


Fig. 4 HPLC chromatograms of reactions catalyzed by Spn-LicC and Ari-PntC (Ari1348). **a** Time-resolved reaction of CTP (open circle) with: I, P-Cho and Spn-LicC to make CDP-Cho (filled circle), and II, AEP and Ari-PntC to generate CMP-AEP (open square). **b** Spn-LicC more readily produces CDP-Cho (panel II) than CMP-AEP (panel III); in contrast, Ari-PntC preferentially generates CMP-AEP (panel IV) compared to CDP-Cho (panel V) after 30 min of reaction time. All reactions contained 50 nM enzyme, 1 mM of either AEP or P-Cho, 4 mM CTP, and 7 mM MgCl₂ in 50 mM Tris-Cl, pH 8.0

Table 1 Steady-state kinetic constants of cytidyltransferases ^a						
Enzyme	Substrate	k_{cat} (s ⁻¹)	K_M (mM)	k_{cat}/K_M (M ⁻¹ s ⁻¹)	Specificity ^b	Ref.
Ari-PntC	AEP	3.7 ± 0.1	0.012 ± 0.001	3.2 × 10 ⁵	0.0023	This work
	ChoP ^c	0.7 ± 0.3	1.0 ± 0.8	7.2 × 10 ²		
Spn-LicC	AEP	0.72 ± 0.05	0.3 ± 0.1	2.3 × 10 ³	200	This work
	ChoP ^d	1.06 ± 0.04	2.4(± 0.6) × 10 ⁻³	4.5 × 10 ⁵		
	ChoP	3.6	0.060	6.0 × 10 ⁴	2700	30
	PEtn	0.031	1.43	22		
	ChoP	17.5	0.39	4.5 × 10 ⁴	5.6 × 10 ⁵	26
	ChoP	37	0.066	5.6 × 10 ⁵		
Tde-PntC	AEP	1.05 ± 0.05	0.016 ± 0.005	6.8 × 10 ⁴	ND	This work
	ChoP	ND ^e	ND	ND		

PEtn phosphoethanolamine
^aStandard errors are included for data generated in this work
^bRatio of specificity constants (k_{cat}/K_M) for ChoP:AEP (or PEtn)
^cSubstrate inhibition observed with $K_S = 4 \pm 1$ mM
^dSubstrate inhibition observed with $K_S = 6.4 \pm 0.9$ mM
^eND, not determined due to low activity

multinuclear NMR (Supplementary Figs. 4–7). Overall, these results clearly demonstrated Ari1348-catalyzed formation of CMP-AEP and imply shared biosynthetic logic for P-Cho and phosphonate tailoring pathways (Fig. 3).

Although activity was observed for each enzyme with its proposed substrate, a comparison of substrate preference further supported our cognate substrate assignments and prompted the adoption of new nomenclature to describe this class of phosphonate-specific enzyme. Previous work revealed a 2700-fold higher specificity constant for Spn-LicC towards P-Cho relative to phosphoethanolamine (Table 1), but activity towards phosphonate substrates was not examined³³. Our HPLC assays

revealed poor cross-reactivity with non-cognate substrates (Fig. 4b). Specifically, Ari1348 clearly preferred AEP over P-Cho under the same conditions, signifying phosphonate cytidyltransferase activity. In addition, both Ari1348 and Tde1415 exhibited strong activity towards CTP, limited activity towards ATP, and no activity detected for GTP (Supplementary Fig. 8). Similar limited reactivity towards ATP was previously observed in the Fom1 CyTase domain²⁸ and Spn-LicC^{32,33}. Based on phosphonate preference and functional analogy to LicC, we propose phosphonyl tailoring cytidyltransferase (PntC) terminology to distinguish these enzymes from P-Cho-specific LicC cytidyltransferases (Fig. 3).

The strict substrate specificity implied by the HPLC analyses of Fig. 4b prompted quantitative investigation via steady-state kinetic analysis. Using a coupled assay to detect pyrophosphate release^{34,35}, our initial rate measurements of Spn-LicC towards P-Cho with saturating concentrations of CTP revealed a k_{cat} of $1.06 \pm 0.04 \text{ s}^{-1}$ and K_{M} of $2.36 \pm 0.65 \mu\text{M}$, affording a $k_{\text{cat}}/K_{\text{M}}$ comparable to previous reports^{29,32,33} (Table 1, Supplementary Fig. 9). In contrast, AEP as a substrate yielded k_{cat} and K_{M} values of $0.723 \pm 0.054 \text{ s}^{-1}$ and $318 \pm 129 \mu\text{M}$, respectively, revealing a 200-fold preference for P-Cho over AEP. Ari-PntC (Ari1348) exhibited the opposite preference, with a 440-fold higher specificity constant for AEP versus P-Cho (Table 1, Supplementary Fig. 9). Similarly, Tde-PntC (Tde1415) was not sufficiently active towards P-Cho to obtain steady-state kinetic data, but activity towards AEP was similar to Ari-PntC (Table 1). Overall, clear preference for AEP as a substrate supports assignment of these enzymes as phosphonate-specific cytidyltransferases, or PntCs.

Molecular determinants of specificity are primarily steric.

Structural studies were undertaken to understand PntC substrate selectivity for AEP versus P-Cho. In contrast to Ari-PntC, the larger two-domain protein Tde1415 was readily crystallized to afford a 2.72 Å structure of the apo enzyme and a 1.95 Å structure of the product complex obtained in the presence of CTP and AEP substrates (Supplementary Table 1). As predicted from gene annotations (Fig. 3c), the overall structure of the enzyme included an N-terminal PntC connected to a C-terminal AEPT domain (Supplementary Fig. 10). The classic type I aminotransferase fold of the AEPT domain is very similar to AEPT from *Salmonella typhimurium*, which is the only other AEPT structure known³⁶. Interestingly, neither of these structures possesses a covalently linked pyridoxal 5'-phosphate (PLP) cofactor, and the colorless Tde1415 solution was consistent with a missing internal aldimine chromophore. To our knowledge, these two enzymes and the alanine-glyoxylate aminotransferase from *Anabaena*³⁷ are the only crystallographic examples of non-covalently bound PLP. Nonetheless, aminotransferase activity was detected as ³¹P NMR chemical shifts consistent with the transformation of AEP to phosphonoacetaldehyde (PnAA, Supplementary Fig. 11) and confirmed by mass spectrometry (Supplementary Fig. 12). The AEPT domain of Tde1415 possesses PLP and the requisite active site features to support classical aminotransferase catalysis (Supplementary Fig. 13).

The crystal structure of the PntC domain of Tde1415 in complex with the CMP-AEP product possesses a binding orientation reminiscent of the previously reported Spn-LicC: CDP-Cho structure (PDB 1JYL, Fig. 5)²⁹. Strikingly, the presence of two adjacent magnesium ions in the Tde-PntC active site contrasts with the single ion observed in the Spn-LicC complex, and each apo-enzyme has one less metal ion. Consistent with our assignment of the metals as magnesium ions, the temperature factors increased from 31.3 to 62.7 Å² when Zn²⁺ was included in crystallographic refinements. In addition, EDTA treatment inactivated Tde1415, but activity was restored by the addition of Mg²⁺ or Zn²⁺ but not Ca²⁺ (Supplementary Fig. 14). Varying metal ion content is well established among phosphate-processing enzymes. For example, a two-magnesium mechanism is favored for CMP-Kdo synthetase (KdsB)^{38,39}, FomD employs two metals for cytidyl (S)-2-hydroxypropylphosphonate hydrolysis⁴⁰, DNA polymerases commonly employ a two-metal ion mechanism with evidence for an additional third divalent metal ion⁴¹, and terpene synthases require three metal ions⁴². Overall, in contrast to Spn-LicC, which loses a salt bridge between Arg129 and a metal-coordinating residue Glu216, the metal coordination

sphere of Tde-PntC does not undergo major changes upon ligand binding (Supplementary Fig. 10).

The crystal structures of Spn-LicC²⁹ and Tde-PntC provide an opportunity to probe the selectivity determinants for respective cognate substrates P-Cho and AEP, which are present in the active sites as CMP-conjugate products. The two substrates clearly differ in size, and possibly in charge; the positive charge of the quaternary amine of P-Cho does not necessarily occur at the primary amine of AEP. Although primary amines are typically positively charged ($\text{pK}_{\text{a}} \sim 10$)⁴³, active site pK_{a} perturbations could occur⁴⁴ to neutralize AEP. However, few clues exist from the Tde-PntC crystal structure, which reveals water, Glu196, and Glu104 positioned to interact with the primary amine of AEP via hydrogen bonds. Intriguingly, the equivalent positions in Spn-LicC (D192 and D105) are occupied by smaller Asp side chains (Fig. 5), which may provide more room to accommodate the larger P-Cho substrate. In addition, Spn-LicC possesses a composite aromatic box for binding the choline quaternary amine via cation- π interactions (Fig. 5)⁴⁵. Notably, Ari-PntC also possesses the equivalent aromatic residues, suggesting that charge may not be a key determinant of P-Cho versus AEP selectivity, and highlighting that Ari-PntC is more closely related to Spn-LicC than Tde-PntC (Supplementary Fig. 15). Therefore, protein cavity volumes were calculated⁴⁶ to evaluate the effects of steric restriction against the larger P-Cho substrate in the Tde-PntC active site. The larger pocket volume of Spn-LicC ($\sim 381 \text{ Å}^3$) compared to Tde-PntC ($\sim 287 \text{ Å}^3$) (Fig. 5) corresponds to the difference of $\sim 64 \text{ Å}^3$ in molecular volume between CDP-Cho and CMP-AEP, or the $\sim 75 \text{ Å}^3$ volume of the choline trimethylamine moiety⁴⁷.

To further probe the effects of steric constraint on substrate selectivity, we pursued molecular dynamics simulations. In addition to the enzyme:product crystal structures of Spn-LicC: CDP-Cho and Tde-PntC: CMP-AEP, we also modeled non-cognate enzyme:product pairs Spn-LicC: CMP-AEP and Tde-PntC: CDP-Cho using $10 \times 150 \text{ ps}$ independent trajectories (1.5 ns in total) for each complex (Fig. 5). Notably, the Tde-PntC active site did not readily accommodate the additional volume of CDP-Cho, and significant conformational changes in the ligand occurred immediately during the simulations. Specifically, the choline moiety was forced towards cytidine, with a concomitant shift in the phosphate backbone enabled by rotation about the ribose C5'-O5' bond. The distribution of this dihedral angle during the Tde-PntC simulations indicates: (i) the magnitude of this shift for the non-cognate ligand CDP-Cho, and (ii) the comparatively narrow distribution of dihedral angles accessed by the cognate ligand CMP-AEP (Fig. 5c). Similar results were obtained for Spn-LicC, characterized by a narrow distribution for the cognate ligand CDP-Cho and a broad bimodal distribution of dihedral angles for the non-cognate CMP-AEP. Insofar as dihedral angle distributions represent movement of the ligand, the narrow distribution of cognate ligand conformations may reflect a more tightly bound ternary complex. Although not observed in the crystal structure, it is possible that a proportion of the LicC:ligand complex in solution would carry an additional Mg²⁺ ion, similar to the observed Tde-PntC: CMP-AEP complex. We therefore also performed simulations with a second Mg²⁺ for both Spn-LicC product complexes, revealing a bimodal distribution of the dihedral for CDP-Cho with a second peak around -150° (Supplementary Fig. 16) and a narrower distribution for CMP-AEP. This may explain why Spn-LicC can accept the non-cognate substrate (e.g. with two Mg²⁺ bound), albeit with increased K_{M} (Table 1) due to the limited interactions of the primary amine in the LicC choline-binding pocket. Overall, the molecular dynamics simulations provided further support for the influence of steric effects on enzyme selectivity.

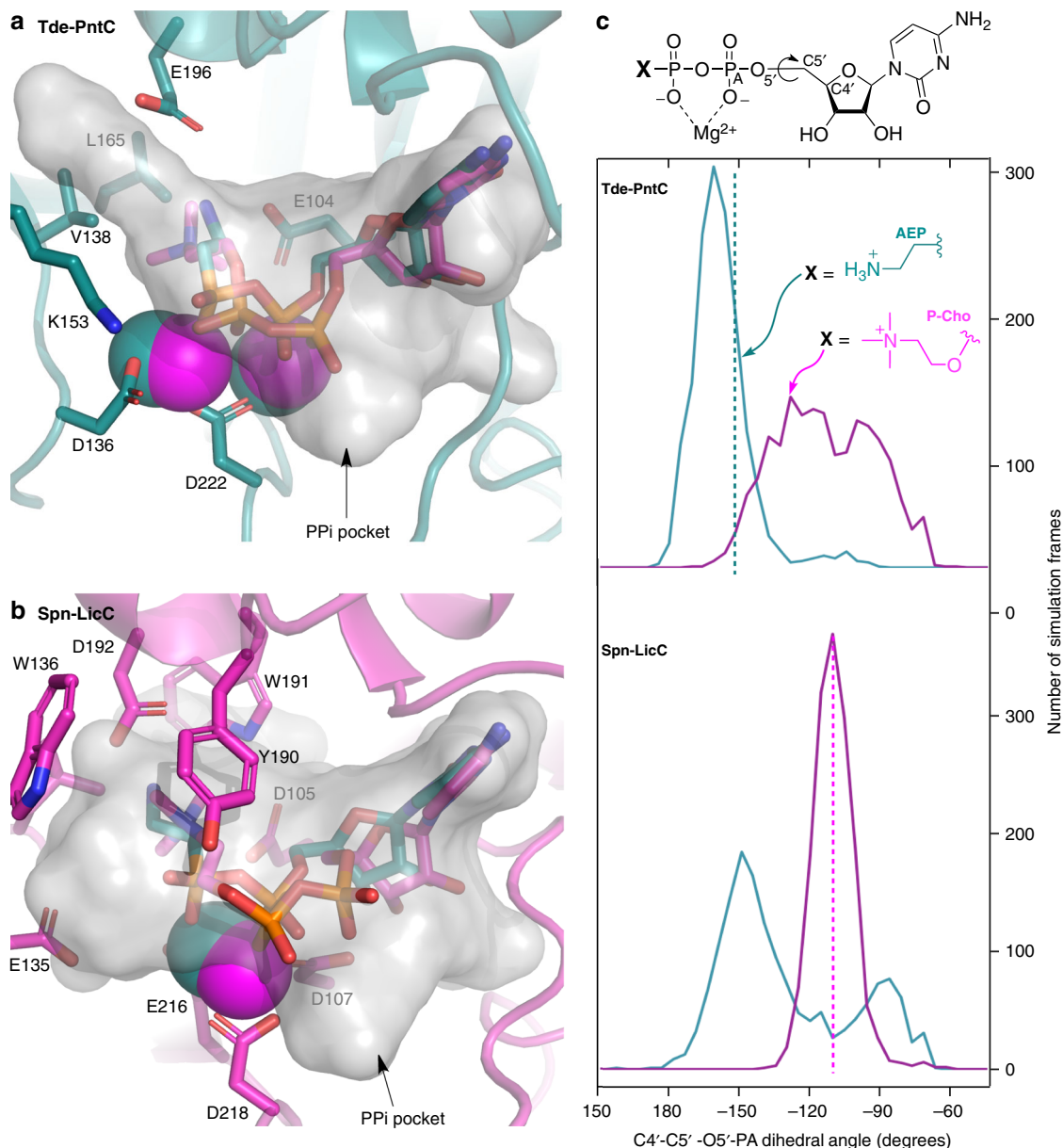


Fig. 5 Molecular dynamics simulations of Tde-PntC (top) and Spn-LicC (bottom). **a** Representative conformations of the Tde-PntC active site with cognate ligand CMP-AEP and Mg²⁺ ions colored teal; non-cognate ligand CDP-Cho and Mg²⁺ ions are magenta. The transparent gray surface representation denotes the 287 Å³ cavity calculated from the crystal structure (minus CMP-AEP) using the Roll algorithm of POCASA⁴². **b** Representative conformations of the Spn-LicC active site showing the cognate ligand CDP-Cho and Mg²⁺ ion colored magenta; non-cognate ligand CMP-AEP and Mg²⁺ are colored teal. Transparent gray surface outlines the 381 Å³ cavity calculated from the 1JYL crystal structure coordinates after removing CDP-Cho (26). **c** Histogram of C4'-C5'-O5'-PA dihedral angles sampled during 10 × 150 ps independent simulations for each protein:ligand pair, using the same color scheme for each ligand (CMP-AEP = teal; CDP-Cho = magenta). Dotted lines represent crystallographically observed dihedral angles

Mechanistic insight from structural data. The crystal structures determined in apo form (PDB 6PD1) and in the presence of CTP and AEP (PDB 6PD2) provide additional mechanistic insight. Electron density outlines the CMP-AEP product (Fig. 6a) with partial density at the expected location of the pyrophosphate (PP_i) leaving group. This PP_i pocket was also detected by the Roll algorithm in both Spn-LicC and Tde-PntC⁴⁶ (Fig. 5a, b). The PP_i site is defined by the first five residues of the GXG(T/S)RX₄₋₈PK nucleotidyltransferase consensus sequence (boxed region, Supplementary Fig. 15)³², which provides stabilizing positive charge via backbone amide protons and the conserved residue Arg15. The terminal Lys25 of the consensus sequence is positioned to interact most strongly with

the magnesium-coordinated α-phosphate of CTP, and alanine substitution of this highly conserved residue abolished cytidyltransferase activity in the related enzymes FrbH (K38A) and YgbP (K27A)^{48,49}. Similar to the Spn-LicC structure, Lys25 appears positioned to accept additional negative charge arising during a pentacoordinate transition state, which would result from nucleophilic attack of AEP in an associative mechanism (Fig. 6b). The partially conserved residue Lys153 may guide attack by interacting with phosphonate oxygen. This mechanistic trajectory was also proposed based on a similar crystallographic orientation of Lys27 in the MEP cytidyltransferase YgbP⁴⁹. Indeed, we observed markedly diminished activities (<10% of wildtype) when alanine was substituted at Arg15,

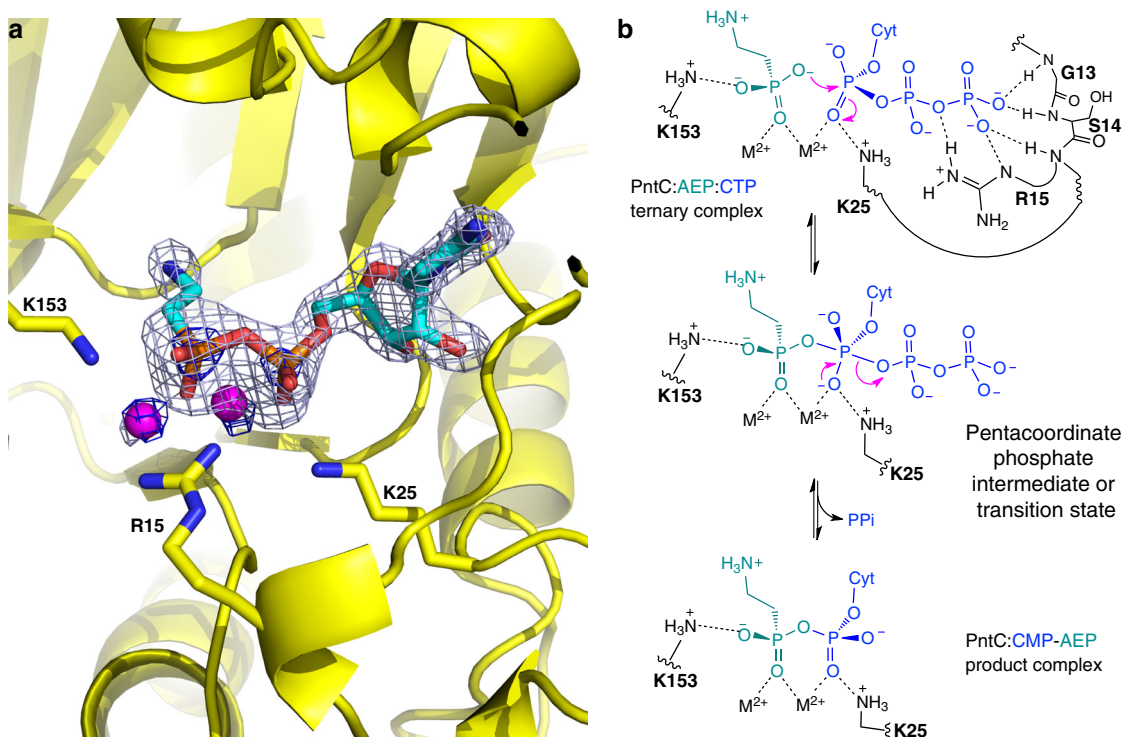


Fig. 6 Proposed mechanism of PntC. **a** CMP-AEP electron density (gray mesh: Fo-Fc omit map contoured at 3.5 sigma; blue mesh: 2Fo-Fc map contoured at 5.0 sigma highlighting the heavier Mg and P atoms) for the Tde-PntC: CMP-AEP complex. **b** Mechanistic interpretation of the crystallographic data. The proposed ternary complex structure (top) with extensive interactions stabilizing the PPi leaving group of CTP (blue). Nucleophilic attack of AEP (teal) generates a pentacoordinate phosphate intermediate or transition state possessing additional negative charge stabilized by Lys25 (middle). In the absence of obvious candidate general base residues, we propose that active site pK_a perturbations may result in the deprotonated AEP substrate shown. Loss of PPi generates the CMP-AEP product bound in the active site (bottom) as seen in the crystal structure in **a**

Lys25, and Lys153 of Tde-PntC (Supplementary Fig. 17), lending support to the mechanism proposed in Fig. 6b. Although detailed kinetic analysis was beyond the scope of this study, we expect that PntC enzymes will employ ordered sequential binding. Previous substrate and product inhibition analyses of Spn-LicC favored CTP as the leading substrate and CDP-Cho as the final product off the enzyme²⁹, and initial CTP binding was concluded from pulse chase analysis of YgbP⁴⁹.

Discussion

We have identified nucleotidyltransferase Pfam families in about two-thirds of phosphonate biosynthetic gene clusters. Surprisingly, about 60% of all Ppm enzymes are fused to one or both of two Pfams, with MobA-like NTP transferase (PF12804) as the most commonly fused domain. Only one member of this family was previously known to act on a phosphonate substrate; FrbH catalyzes cytidyltransfer to L-2-amino-4-phosphonobutyrate during FR-900098 biosynthesis⁴⁸. The other commonly fused domain is cytidyltransferase-like (PF01467), which includes the PhpF phosphonoformate cytidyltransferase functioning in phosphinothricin biosynthesis⁵⁰ and the Fom1 HEP cytidyltransferase from the fosfomycin biosynthetic pathway²⁸. In demonstrating AEP-specific cytidyltransferase activity for two PF12804 enzymes, we have expanded the catalytic repertoire of this family to include phosphoryl tailoring cytidyltransferases (PntCs) involved in putative cell surface tailoring pathways.

Cytidyl activation has been well documented in the biosynthesis of cell surface glycans and phospholipids, but is rare in natural product biosynthesis. Indeed, we are not aware of examples beyond small molecule phosphonates and the MEP pathway (e.g. YgbP of the IspD family) for terpenoid biosynthesis.

In contrast, CMP-activated sialic, legionaminic, pseudaminic acids, as well as CMP-Kdo, exemplify common intermediates in cell surface glycan biosynthesis^{38,51}. Similarly, CMP-conjugates facilitate phospholipid biosynthesis, including CDP-diacylglycerol and the aforementioned CDP-choline^{52,53}. The significance of cytidyltransferase-enrichment in phosphonate biosynthesis is unclear, but may simply reflect that most phosphonates occur on cell surface glycans and lipids.

We expect that PntC enzymes will activate a variety of phosphonates to furnish a mosaic of cell surface phosphonate chemistry. Identifying CMP-conjugates will enable discovery of new phosphoryl modifications and elucidation of their biological roles. Further examples of related chemical logic in biosynthetic pathways, such as AEP and the virulence factor P-Cho, will present opportunities to understand and manipulate enzyme selectivity for developing biocatalysts and selective antivirulence agents.

Methods

General. CTP was purchased from Thermo Fisher Scientific (Mississauga, ON, Canada). Chelex 100 sodium form (50–100 mesh), AEP, P-Cho, and CDP-Cho were purchased from Sigma-Aldrich (Oakville, ON, Canada). P-Cho was treated with Chelex 100 resin as previously described prior to use in order to remove calcium, which inhibits the enzyme³². All other chemicals were used without further purification. DNA sequencing was performed at The Centre for Applied Genomics at the Hospital for Sick Children (Toronto, ON, Canada). HR-ESI-MS was performed at the Alberta Glycomics Centre (Edmonton, AB, Canada). HPLC analysis was performed using a Prominence LC-20AT system equipped with a diode array detector (Shimadzu, Kyoto, Japan). FPLC purifications were performed using an NGC™ Chromatography System (Bio-Rad, Mississauga, ON). NMR spectra were recorded on an Agilent DD2 operating at 400 MHz for ¹H and 100 MHz for ¹³C. A Varian Unity Inova operating at 121 MHz was used to record ³¹P NMR spectra.

Establishing hidden Markov models. Ppm protein sequences were retrieved from NCBI with the following accession numbers: *Tetrahymena pyriformis* (P33182); FrbD from *Streptomyces rubellomurinus* (ABB90393); *Bacillus subtilis* subsp. spizizenii str. W23 (WP_003223692); *Streptomyces viridochromogenes* (AAU00071); *Streptomyces lividus* (ACZ13456); *S. wedmorensis* (BAA32495); *Streptomyces fra-diae* (ACG70831); *Pseudomonas syringae* (AFM38986). Cytidyltransferase (PntC) protein sequences were retrieved from NCBI with the following accession numbers: Tde-PntC from *T. denticola* ATCC 35405 (NP_992021); Oul-PntC from *O. uli* DSM 7084 (ADK67708); Ari-PntC from *A. rimae* ATCC 49626 (ZP_03568201). The retrieved sequences were used to collect representative HMMs for Ppm and putative PntC enzymes from the Pfam database using the HMMER software suite^{54,55}. The GA (gathering) score thresholds were applied for determining matches, which is considered a reliable curated threshold for defining family membership⁵⁵.

Retrieving Ppm and PntC homologs from HMMs. HMMs matching the retrieved Ppm and PntC mentioned above (for Ppm: PF13714; for PntC: PF12804, PF00483, PF01129) were used to scan collectively annotated protein sequences from the NCBI RefSeq genome databases⁵⁶ of complete genomes ($n = 8582$), genome scaffolds ($n = 41,568$), and contigs ($n = 60,795$), using HMMScan. After potential homologs were thus identified, a Python script was written and used to narrow the results into homologs sharing alignment to at least one of the HMMs for PntC and the single HMM retrieved for Ppm. To improve accuracy of the search, results were filtered to ensure that only sequences with $\geq 60\%$ alignment to the HMMs were included. Ppm homologs were further screened to ensure the presence of the conserved catalytic motif EDKXXXXXNS, which distinguishes PEP mutase from other members of the isocitrate lyase family⁴.

Inventory of Ppm fusion domains. Protein sequences were retrieved for all identified Ppm homologs from NCBI RefSeq genome databases and scanned for HMMs using the HMMER software suite to establish an inventory of fusion domains. The GA (gathering score) threshold was once again applied for determining family membership. A Perl script was applied to account for overlapping domains. In the case of overlapping domains, only the domain with the highest score was included in analysis. Results were also filtered with $\geq 60\%$ alignment to the HMMs as described above.

Distribution of distances between ppm and pntC genes. A Python script was written to calculate distances, in number of genes, between *ppm* and *pntC* homologs (after filtering for $\geq 60\%$ HMM alignment and presence of Ppm motif) in complete, contig, and scaffold NCBI RefSeq genome databases. If multiple *ppm* or *pntC* were present in one genome/contig, only the closest distance was tabulated. To further limit the results to non-redundant genomes (one per species), the genome database was filtered using tri-nucleotide DNA signatures as reported previously⁵⁷. The genomes were filtered at a distance $\Delta = 0.03$, which roughly corresponds to species.

Sequence alignment and homology modeling. The following amino acid sequences were retrieved from NCBI and submitted to the Clustal Omega website for alignment:⁵⁸ Bfr-PntC from *B. fragilis* 638R (CBW22390); Tde-PntC from *T. denticola* ATCC 35405 (NP_992021); Cj1416 from *Campylobacter jejuni* (CAI38904); Oul-PntC from *O. uli* DSM 7084 (ADK67708); Ari-PntC from *A. rimae* ATCC 49626 (ZP_03568201); Spn-LicC from *S. pneumoniae* R36A (AAK94072); Hin-LicC from *Haemophilus influenzae* C486 (AJO89865). Homology models were generated via amino acid sequence submission to the I-TASSER server⁵⁹. Protein pocket sizes were calculated using the Roll algorithm of the web-based POCASA program after deleting the CMP-conjugate ligand but not metal cofactor(s)⁴⁶.

Molecular dynamics simulations. The crystal structures of 1JYL (chain D) and 6PD2 (focusing on the chain B active site of the BD dimer) were used with experimental coordinates for cognate substrates CDP-Cho and CMP-AEP, respectively. Non-cognate substrates (i.e. 1JYL:CDP-AEP and 6PD2:CDP-Cho) were built in PyMOL⁶⁰. The Enlighten plugin for PyMOL was used to execute protocols using AmberTools14 software for ligand parameterization with GAFF⁶¹, hydrogen and solvent addition (PREP protocol), structure relaxation and minimization (STRUCT protocol), and molecular dynamics (MD at 300 K; DYNAM protocol)⁶². All simulated active site residues were in their standard protonation states; Tde1415 histidines within the solvated simulation sphere were protonated as follows: HIE57, HID186, HIE187, HIE197, and HIE226. For each of the four complexes, 10 independent 150 ps MD simulations were run using a 20 Å solvent shell surrounding P_A atom (equivalent of CTP α -phosphate P) of the substrate. From the 1500 ps of simulation data for each complex, dihedral angles were measured every 1 ps using the cpptraj program included in AmberTools⁶³. The simulation data was clustered using cpptraj (hierarchical agglomerative clustering on the RMSD of the substrate, with $\epsilon = 0.85$ for all complexes except for Tde-PntC: P-Cho complex, which used $\epsilon = 1.1$) to identify centroid conformations that were representative of most common conformations observed.

Bacterial strains and media. *Escherichia coli* BL21(DE3) and *E. coli* DH5a (Supplementary Table 2) from Life Technologies (Carlsbad, CA) were used for protein production and cloning, respectively, and were cultured in standard LB broth. The *spn-licC* gene was purchased from BioBasic Canada (Markham, ON) in the pET57 vector to include the N-terminal sequence MGSSSH₆SSGLVPRGSH prior to the N-terminal methionine residue and preserve the exact sequence of the previously characterized enzyme^{29,33}. The synthetic *spn-licC* gene was directly cloned as an *NdeI/XhoI* fragment into pET29 to afford pGH1000. The *ari1348* gene was purchased codon-optimized for *E. coli* from BioBasic in the pET28a vector and subcloned as an *NdeI/NotI* fragment into pET29. The resulting pGH2000 expression construct is designed to generate C-terminal His₆-tagged Ari-PntC protein. The *tde1415* gene was purchased from BioBasic in pET28a and subcloned without its stop codon as a *NdeI/NotI* fragment into pET21b to afford pGH3000 for producing C-terminal histidine-tagged protein. Constructs are summarized in Supplementary Table 3. *A. rimae* (ATCC[®] 49626TM) and *O. uli* ATCC[®] 49627TM were purchased from Cedarlane Labs (Burlington, ON, Canada) and grown in PYG broth plus 0.1% (v/v) Tween 80 (ATCC[®] medium 1482) from Anaerobe Systems (Morgan Hill, CA). Anaerobic media for these two organisms was either reduced by incorporating 1 g/L L-cysteine hydrochloride (Fisher Scientific, Hampton, NH) in the media or through incubation (minimum of 24 h) in a Bactron II Anaerobic Chamber (Sheldon Manufacturing Inc., Cornelius, OR) containing an anaerobic gas mixture (consisting of 5% CO₂, 5% H₂, and the balance N₂ supplied by Praxair). *O. uli* and *A. rimae* were grown to stationary phase (~48 h) in the anaerobic chamber at 37 °C in a stationary batch format of 1 L culture volumes.

RT-PCR analysis. Gene transcription was monitored with primers outlined in Supplementary Table 4. RNA extraction from bacteria was performed using the Ribopure RNA isolation kit (Invitrogen, Carlsbad, CA). Any remaining genomic DNA that may have been carried through the RNA extraction process was removed with a 1 h DNaseI treatment step, which was included in the kit. Following RNA extraction and DNaseI treatment, a DNA-based PCR was always performed to detect undigested DNA. The lack of amplification products confirmed the absence of contaminating genomic DNA. RT-PCR was carried out using the OneStep RT-PCR kit (Qiagen) according to the manufacturer's recommendations. Briefly, each reaction setup consisted of 2 μ l of dNTP mix (400 μ M of each dNTP in a reaction), 0.6 μ M of each primer, 2 μ l of polymerase mix and 2 μ l of specific RNA templates. The thermal cycling protocol was performed with the iCycler iQ multicolor real-time detection system (Bio-Rad, Hercules, CA) and contained an initial reverse transcription step of 50 °C for 30 min followed by PCR activation at 95 °C for 15 min. Subsequent steps in the protocol contained 40 cycles of amplification (94 °C for 45 s, 55 °C for 45 s, 72 °C for 1 min) and a concluding step at 72 °C for 10 min. Amplified products were analyzed on 1.8% (w/v) agarose gels stained with 0.5 μ g/ml ethidium bromide and imaged with a VersaDocTM 4000 MP (BioRad).

Site-directed mutagenesis and analysis of mutants. Tde1415 enzyme variants R15A, K25A, and K153 were generated by overlap extension PCR mutagenesis using primers listed in Supplementary Table 4. All mutants were verified by sequencing and proteins expressed in pET21b. Activity of enzyme variants was monitored by ³¹P NMR after 2 h incubation at room temperature in 50 mM Tris-Cl pH 8.0 containing 7.0 mM CTP, 3 mM AEP, 10 μ M Tde1415, and 7.0 mM of MgCl₂. Phosphonoacetic acid at 6.0 mM was added as an internal standard immediately prior to ³¹P NMR spectral acquisition.

Protein production. Plasmids were transformed into *E. coli* BL21(DE3) and plated on the LB agar plates containing the appropriate antibiotic. Single colonies were picked into ~5 ml and grown overnight at 37 °C in LB supplemented with antibiotic, 1 ml of which was then transferred to 50 ml LB supplemented with antibiotic. After overnight growth at 37 °C, 11 batches of fresh LB were inoculated with 10 ml of the overnight culture and incubated at 37 °C and 220 rpm. At OD₆₀₀ ~0.5, cultures were cooled on ice to ~18 °C, supplemented with 0.1 mM IPTG, and then incubated overnight at 18 °C. Cells were harvested by 15 min centrifugation at 4 °C and 4000 \times g and subsequent steps were performed on ice. From 1 L of culture, the resulting pellet was resuspended in cell lysis buffer (50 ml, 0.73 M sucrose, 50 mM Tris-Cl, pH 8.0) and supplemented with 4 mM dithiothreitol (DTT, Amresco, Solon, OH). Egg white lysozyme (1 mg, Amresco) was added and stirred for 10 min, after which deoxycholate solution (50 ml) was added and the solution was stirred until it became viscous (~10 min). The deoxycholate solution contained 24 mM deoxycholate sodium salt (BioBasic, Markham, ON), 0.5% v/v Triton X-100 (BioBasic), 20 mM Tris-Cl, pH 8.0, 0.3 M NaCl. A solution of 1 M MgCl₂ (500 μ l) was added together with deoxyribonuclease I from bovine pancreas (Sigma-Aldrich) and stirred at room temperature until the solution became less viscous. The solution was then centrifuged at high speed (14,000 \times g) for 20 min at 4 °C to afford clarified supernatant raw extract.

Protein purification. To each 50 ml of raw extract was added 2 ml of Ni-NTA agarose affinity resin (QIAGEN, Hilden, Germany) and gently shaken at 4 °C and 120 rpm for 40 min. The resin was then washed and eluted with 20 and 250 mM imidazole, respectively, in 50 mM Tris-Cl buffer pH 8.0 containing 300 mM NaCl. Eluted protein (10 ml) was dialyzed overnight at 4 °C in 50 mM Tris-Cl, pH 8.0

using MWCO 3500 dialysis tubing, and then run over a HiTrap Q FF anion exchange column (GE Healthcare, Chicago, IL) attached to an NGC FPLC system (Bio-Rad, Hercules, CA). After isocratic flow in 50 mM Tris-Cl (pH 8.0) for 2.5 column volumes, a linear gradient from 0 to 700 mM NaCl was performed over 18 column volumes. Tde1415 eluted at ~120 mM NaCl, and Ari1348 eluted at ~250 mM NaCl, consistent with the respective predicted *pI* values of 5.7 and 5.0 as calculated using the ProtParam tool on the ExPASy web server⁶⁴. Pooled FPLC fractions were concentrated to ~2 ml by ultrafiltration using 10 kDa MWCO centrifugation filters (Pall Corporation, Port Washington, NY), then desalted into Tris-Cl pH 8.0 buffer using PD-10 columns (GE Healthcare). The desalted protein was concentrated to ~200 µl by ultrafiltration, then either used immediately or frozen as beads in liquid nitrogen for storage at -80 °C until further use.

Protein analysis. Protein concentrations were estimated using the Bradford assay⁶⁵, and purity was assessed using SDS-PAGE. Oligomeric structure was evaluated using size-exclusion chromatography and DLS. The former was performed on a Bio-Rad NGC FPLC system equipped with a Superdex 75 10/300 GL column from GE Healthcare, eluted using an isocratic flow (0.5 ml/min) of 50 mM Tris-Cl and 150 mM MgCl₂ at pH 8.0. DLS was performed on 20 µl of freshly purified protein (8 mg/ml) at 20 °C using a DynaPro NanoStar (Wyatt Technology, Santa Barbara, CA).

HPLC enzyme assays. Reactions containing 50 nM enzyme, 1 mM of either AEP or P-Cho, 4 mM CTP, 7 mM MgCl₂, and 50 mM Tris-Cl pH 7.8 were allowed to proceed for 30 min prior to quenching a 10 µl aliquot with an equal volume of cold methanol (containing 0.1% TFA). The quenched reaction was centrifuged for 5 min prior to injecting 1 µl on an HPLC equipped with a Luna NH₂ column (3 µm, 100 Å, 100 × 4.6 mm, Phenomenex, Torrance CA, USA) using an isocratic elution at 1 ml/min in a mobile phase of 20 mM ammonium acetate, pH 10.

Aminotransferase activity assays. The AEPT activity was observed by combining 1.5 mM AEP, 6 mM pyruvate, 30 µM pyridoxal-5'-phosphate (PLP) in 50 mM Tris-Cl buffer containing 50 mM MgCl₂, pH 8.0. The reaction was initiated by adding 1 µM of Tde1415 enzyme, which was missing in the no-enzyme negative control. The reaction was either monitored directly via ³¹P NMR as shown in Supplementary Fig. 11 or allowed to proceed at room temperature for 2 h prior to removal of enzyme by ultrafiltration using a Vivaspin 5000 Da MWCO membrane centrifugation device (Sartorius, Goettingen, Germany). Filtrate was stored frozen at -20 °C prior to mass spectrometric analysis at the Mass Spectrometry Facility at the University of Guelph (Supplementary Fig. 12).

Metal use assays. 140 µl of 400 µM recombinant wildtype Tde1415 was diluted to a volume of 3.0 ml with 50 mM EDTA, 50 mM Tris-HCl, pH 8.0 buffer. The protein solution was applied to an Econo-Pac 10DG desalting column (Bio-Rad) and exchanged into 50 mM EDTA, 50 mM Tris-Cl, pH 8.0 buffer. The eluted protein was concentrated using a 5 kDa MWCO ultracentrifuge device (Sartorius) and then desalted a second time into 50 mM Tris-Cl, pH 8.0. The de-metalated protein was again concentrated to 2.0 ml by ultracentrifugation and stored at 4 °C. PntC activity was monitored by ³¹P NMR after 2 h incubation at room temperature in 50 mM Tris-Cl pH 8.0 containing 7.0 mM CTP, 3 mM AEP, 5.5 µM Tde1415, and 7.0 mM of divalent metal (MgCl₂, CaCl₂, or ZnCl₂). Phosphonoacetic acid at 6.0 mM was added as an internal standard immediately prior to ³¹P NMR spectral acquisition.

Colorimetric coupled enzyme assays. The EnzCheck® Pyrophosphate Assay Kit (Molecular Probes, Inc., Eugene, OR, USA) was used to determine the activity of Spn-LicC, Ari-PntC, and Tde1415. Each reaction was kept to a total volume of 100 µl and performed in triplicate. The reaction components were split between two wells, one well contained the substrate and enzyme, while the other well contained CTP. Well 1 contained 0.5 µl (1U) PNP, 0.5 µl (0.03U) IPP, 10 µl (0.2 mM) MESG, 2.5 µl 20X reaction buffer, 16 µl (4 mM) CTP, and 20.5 µl of water, making a total of 50 µl. Well 2 contained 0.5 µl (1U) PNP, 0.5 µl (0.03U) IPP, 10 µl (0.2 mM) MESG, 2.5 µl 20X reaction buffer, 12 µl (7 mM) MgCl₂, enzyme (variable), substrate (variable), and H₂O to fill to a final volume of 50 µl. A control with either no enzyme or substrate was made for each trial. The separate wells were incubated for 30 min at room temperature. After 30 min, well 2 was combined to well 1, and absorbance was recorded every 30 s at 360 nm for 30 min. Initial velocities (<10% substrate turnover) for each substrate concentration were exported to Excel and Michaelis-Menten and substrate inhibition equations were fit by non-linear regression using the R software⁶⁶.

Purification of CMP-AEP. 5 ml reactions containing 1 µM Ari-PntC, 1 mM of AEP, 2 mM CTP, 7 mM MgCl₂, and 50 mM Tris-Cl pH 8 were allowed to proceed for 1 h at room temperature prior to removing the enzyme through centrifugation in a 5 kDa ultracentrifugation tube. The flow-through was injected on the FPLC over a 5 ml GE Hi-Trap™ Q FF anion exchange column into the mobile phase A (25 mM ammonium bicarbonate pH 9) and eluted using a linear gradient of 0–70% mobile phase B (25 mM ammonium bicarbonate + 1 M NaCl pH 9). Peak fractions pertaining to the CMP-AEP product were collected and lyophilized to a dry solid.

20–25 mg of the lyophilized product was dissolved into 600 µl of D₂O before subsequent ¹H, ¹³C, and ³¹P experiments were performed. Phosphonoacetic acid was added as an internal standard for the ³¹P experiments.

Protein crystallization. Purified Tde1415 in 50 mM Tris-Cl, pH 8.0 and 240 mM NaCl, were concentrated to 20 mg/ml with and without presence of 5 mM CTP/5 mM AEP. Tde1415 was initially screened against commercially available sparse-matrix screens in a 1:1 ratio, 1 µl final volume using an ARI Crystal Gryphon (Art Robins Instruments). The microplates were sealed, incubated at 18 °C, and conditions in which crystal growth was observed were used to design hanging-drop vapor diffusion expansion crystal plates. The ligand-free structure was determined by crystals grown against a crystallization solution composed of 0.01 M nickel II chloride hexahydrate, 0.1 M Tris-Cl, pH 8.5, 1.0 M lithium sulfate monohydrate and cryoprotected with an equivalent solution supplemented with 30% (v/v) glycerol. The product complex was determined from a crystal grown against a crystallization solution composed of 0.2 M magnesium acetate tetrahydrate, 0.1 M sodium cacodylate trihydrate pH 6.5, 20% (w/v) polyethylene glycol 8000 cryoprotected with an equivalent solution supplemented with 30% (v/v) glycerol.

X-ray data collection and processing. Protein crystals were retrieved, briefly introduced in cryoprotectant, and snap-frozen in liquid nitrogen. Data analysis was performed at the Advanced Photon Source (APS) at Argonne National Laboratory (Argonne, Illinois, Illinois & Michigan Canal State Trail, 9700 Cass Ave, Lemont, IL 60439, USA) and the Canadian Light Source (CLS) at the University of Saskatchewan (Saskatoon, Saskatchewan, Canadian Light Source Inc., 44 Innovation Boulevard, SK S7N 2V3, Canada). At the APS, X-ray diffraction data was collected at beamline 17-ID of the Argonne National Laboratory Synchrotron Facility. At the CLS, X-ray diffraction data was collected at beamline CLS-08-ID. In both cases images were collected using 0.25 oscillations at a temperature of 100 K and wavelength of 0.9795 nm. Data were indexed and scaled using AutoProcess in the space group P2₁ and data processed to 2.72 Å resolution. Note that while both datasets belong to the P2₁ space group, the unit cell dimensions were different. The “apo” structure of Tde1415 was solved via molecular replacement using the program PHASER⁶⁷ searching for four copies of PDB coordinates 1JYK²⁹ and 1VJO³⁷ which are the cytidyltransferase LicC from *S. pneumoniae* and an alanine-glyoxylate aminotransferase from *Anabaena [Nostoc.]* sp. PCC 7120, respectively. Cycles of iterative model building, structure refinement, and density modification were performed with PHENIX⁶⁸ and were interspersed with inspection and manual building with COOT⁶⁹. Restraints for CDP-Cho were generated via the Grade Web Server (<http://grade.globalphasing.org>). Ramachandran analysis of the apo structure revealed: 2288 (94.1%) torsion angles in the preferred region, 119 (4.9%) allowed, and 25 (1.0%) disallowed; for the Tde1415:CMP-AEP complex: 2325 (95.1%) preferred, 98 (4.0%) allowed, 21 (0.9%) disallowed.

Reporting summary. Further information on research design is available in the Nature Research Reporting Summary linked to this article.

Data availability

The authors declare that the data supporting the findings of this study are available within the paper and its supplementary information files of in a public repository. Specifically, associated raw data has been provided as a source data file for Supplementary Figs. 1, 2, 9, 14, and 17. The coordinates and structure factors of Tde1415 and Tde1415:CMP-AEP have been deposited in the Protein Data Bank with respective PDB accession codes 6PD1 and 6PD2. Other data are available from the corresponding author upon reasonable request.

Code availability

Bioinformatic scripts are available at GitHub: <https://github.com/papi0310/ppm-pntC-clustering>

Received: 4 December 2018 Accepted: 25 July 2019

Published online: 16 August 2019

References

- Horiguchi, M. & Kandatsu, M. Isolation of 2-aminoethane phosphonic acid from rumen protozoa. *Nature* **184**, 901–902 (1959).
- Horsman, G. P. & Zechel, D. L. Phosphonate biochemistry. *Chem. Rev.* **117**, 5704–5783 (2017).
- Metcalfe, W. W. & van der Donk, W. A. Biosynthesis of phosphonic and phosphinic acid natural products. *Annu. Rev. Biochem.* **78**, 65–94 (2009).
- Yu, X. et al. Diversity and abundance of phosphonate biosynthetic genes in nature. *Proc. Natl Acad. Sci. USA* **110**, 20759–20764 (2013).
- Ju, K.-S., Doroghazi, J. R. & Metcalfe, W. W. Genomics-enabled discovery of phosphonate natural products and their biosynthetic pathways. *J. Ind. Microbiol. Biotechnol.* **41**, 345–356 (2014).

6. Ju, K.-S. et al. Discovery of phosphonic acid natural products by mining the genomes of 10,000 actinomycetes. *Proc. Natl Acad. Sci USA* **112**, 12175–12180 (2015).
7. Bowman, Elise, McQueney, Michael, Barry, R. J. & Dunaway-Mariano, Debra Catalysis and thermodynamics of the phosphoenolpyruvate/phosphonopyruvate rearrangement. Entry into the phosphonate class of naturally occurring organophosphorus compounds. *J. Am. Chem. Soc.* **110**, 5575–5576 (1988).
8. Chi, M. C. & Horsman, G. P. Evaporative light scattering quantification of natural products possessing a carbon-phosphorus bond. *J. Antibiot.* **68**, 752–756 (2015).
9. Peck, S. C. & van der Donk, W. A. Phosphonate biosynthesis and catabolism: a treasure trove of unusual enzymology. *Curr. Opin. Chem. Biol.* **17**, 580–588 (2013).
10. Baumann, H., Tzianabos, A. O., Brisson, J. R., Kasper, D. L. & Jennings, H. J. Structural elucidation of two capsular polysaccharides from one strain of *Bacteroides fragilis* using high-resolution NMR spectroscopy. *Biochemistry* **31**, 4081–4089 (1992).
11. Ha, R. et al. Accumulation of peptidoglycan O-acetylation leads to altered cell wall biochemistry and negatively impacts pathogenesis factors of *Campylobacter jejuni*. *J. Biol. Chem.* **291**, 22686–22702 (2016).
12. Hager, F. F. et al. Functional characterization of enzymatic steps involved in pyruvylation of bacterial secondary cell wall polymer fragments. *Front. Microbiol.* **9**, 1356 (2018).
13. Thongsomboon, W. et al. Phosphoethanolamine cellulose: a naturally produced chemically modified cellulose. *Science* **359**, 334–338 (2018).
14. Zughaier, S. M., Kandler, J. L., Balthazar, J. T. & Shafer, W. M. Phosphoethanolamine modification of *Neisseria gonorrhoeae* lipid A reduces autophagy flux in macrophages. *PLoS One* **10**, e0144347 (2015).
15. Clark, S. E. & Weiser, J. N. Microbial modulation of host immunity with the small molecule phosphorylcholine. *Infect. Immun.* **81**, 392–401 (2013).
16. Clark, S. E., Snow, J., Li, J., Zola, T. A. & Weiser, J. N. Phosphorylcholine allows for evasion of bactericidal antibody by *Haemophilus influenzae*. *PLoS Pathog.* **8**, e1002521 (2012).
17. Weiser, J. N. et al. Phosphorylcholine on the lipopolysaccharide of *Haemophilus influenzae* contributes to persistence in the respiratory tract and sensitivity to serum killing mediated by C-reactive protein. *J. Exp. Med.* **187**, 631–640 (1998).
18. Young, N. M., Foote, S. J. & Wakarchuk, W. W. Review of phosphocholine substituents on bacterial pathogen glycans: synthesis, structures and interactions with host proteins. *Mol. Immunol.* **56**, 563–573 (2013).
19. Kharat, A. S. & Tomasz, A. Drastic reduction in the virulence of *Streptococcus pneumoniae* expressing type 2 capsular polysaccharide but lacking choline residues in the cell wall. *Mol. Microbiol.* **60**, 93–107 (2006).
20. Gehre, F. et al. Role of teichoic acid choline moieties in the virulence of *Streptococcus pneumoniae*. *Infect. Immun.* **77**, 2824–2831 (2009).
21. Zeng, X.-F. et al. A C-terminal truncated mutation of licC attenuates the virulence of *Streptococcus pneumoniae*. *Res. Microbiol.* **165**, 630–638 (2014).
22. Bartlett, C. et al. Whole-cell detection of C–P bonds in bacteria. *Biochemistry* **56**, 5870–5873 (2017).
23. Göker, M. et al. Complete genome sequence of *Olsenella uli* type strain (VPI D76D-27CT). *Stand. Genom. Sci.* **3**, 76–84 (2010).
24. Parahitiyawa, N. B. et al. Clonality of bacterial consortia in root canals and subjacent gingival crevices. *J. Investig. Clin. Dent.* **6**, 32–39 (2015).
25. Frederick, J. R., Sarkar, J., McDowell, J. V. & Marconi, R. T. Molecular signaling mechanisms of the periopathogen, *Treponema denticola*. *J. Dent. Res.* **90**, 1155–1163 (2011).
26. Zhang, G., Dai, J., Lu, Z. & Dunaway-Mariano, D. The phosphonopyruvate decarboxylase from *Bacteroides fragilis*. *J. Biol. Chem.* **278**, 41302–41308 (2003).
27. Kim, A. D. et al. The 2-aminoethylphosphonate-specific transaminase of the 2-aminoethylphosphonate degradation pathway. *J. Bacteriol.* **184**, 4134–4140 (2002).
28. Cho, S.-H. et al. Fosfomycin biosynthesis via transient cytidylation of 2-hydroxyethylphosphonate by the bifunctional Fom1 enzyme. *ACS Chem. Biol.* **12**, 2209–2215 (2017).
29. Kwak, B.-Y. et al. Structure and mechanism of CTP:phosphocholine cytidyltransferase (LicC) from *Streptococcus pneumoniae*. *J. Biol. Chem.* **277**, 4343–4350 (2002).
30. Ballouz, S., Francis, A. R., Lan, R. & Tanaka, M. M. Conditions for the evolution of gene clusters in bacterial genomes. *PLoS Comput. Biol.* **6**, e1000672 (2010).
31. Denapaite, D., Brückner, R., Hakenbeck, R. & Vollmer, W. Biosynthesis of teichoic acids in *Streptococcus pneumoniae* and closely related species: lessons from genomes. *Microb. Drug Resist.* **18**, 344–358 (2012).
32. Campbell, H. A. & Kent, C. The CTP:phosphocholine cytidyltransferase encoded by the licC gene of *Streptococcus pneumoniae*: cloning, expression, purification, and characterization. *Biochim. Biophys. Acta* **1534**, 85–95 (2001).
33. Rock, C. O., Heath, R. J., Park, H. W. & Jackowski, S. The licC gene of *Streptococcus pneumoniae* encodes a CTP:phosphocholine cytidyltransferase. *J. Bacteriol.* **183**, 4927–4931 (2001).
34. Suárez, A. S. G., Stefan, A., Lemma, S., Conte, E. & Hochkoeppler, A. Continuous enzyme-coupled assay of phosphate- or pyrophosphate-releasing enzymes. *BioTechniques* **53**, 99–103 (2012).
35. Webb, M. R. A continuous spectrophotometric assay for inorganic phosphate and for measuring phosphate release kinetics in biological systems. *Proc. Natl Acad. Sci. USA* **89**, 4884–4887 (1992).
36. Chen, C. C. H. et al. Degradation pathway of the phosphonate ciliate: crystal structure of 2-aminoethylphosphonate transaminase. *Biochemistry* **41**, 13162–13169 (2002).
37. Han, G. W. et al. Crystal structure of an alanine-glyoxylate aminotransferase from *Anabaena* sp. at 1.70 Å resolution reveals a noncovalently linked PLP cofactor. *Proteins* **58**, 971–975 (2005).
38. Heyes, D. J. et al. Structure-based mechanism of CMP-2-keto-3-deoxymanno-octulonic acid synthetase: convergent evolution of a sugar-activating enzyme with DNA/RNA polymerases. *J. Biol. Chem.* **284**, 35514–35523 (2009).
39. Schmidt, H. et al. Evidence for a two-metal-ion mechanism in the cytidyltransferase KdsB, an enzyme involved in lipopolysaccharide biosynthesis. *PLoS ONE* **6**, e23231 (2011).
40. Sato, S. et al. Biochemical and structural analysis of FomD that catalyzes the hydrolysis of cytidyl (S)-2-hydroxypropylphosphonate in fosfomycin biosynthesis. *Biochemistry* **57**, 4858–4866 (2018).
41. Raper, A. T., Reed, A. J. & Suo, Z. Kinetic mechanism of DNA polymerases: contributions of conformational dynamics and a third divalent metal ion. *Chem. Rev.* **118**, 6000–6025 (2018).
42. Christianson, D. W. Structural and chemical biology of terpenoid cyclases. *Chem. Rev.* **117**, 11570–11648 (2017).
43. Bryantsev, V. S., Diallo, M. S. & Goddard, W. A. pKa calculations of aliphatic amines, diamines, and aminoamides via density functional theory with a Poisson–Boltzmann continuum solvent model. *J. Phys. Chem. A* **111**, 4422–4430 (2007).
44. Harris, T. K. & Turner, G. J. Structural basis of perturbed pKa values of catalytic groups in enzyme active sites. *IUBMB Life* **53**, 85–98 (2002).
45. Nagy, G. N. et al. Composite aromatic boxes for enzymatic transformations of quaternary ammonium substrates. *Angew. Chem. Int. Ed. Engl.* **53**, 13471–13476 (2014).
46. Yu, J., Zhou, Y., Tanaka, I. & Yao, M. Roll: a new algorithm for the detection of protein pockets and cavities with a rolling probe sphere. *Bioinformatics* **26**, 46–52 (2010).
47. Molinspiration Cheminformatics. Calculation of molecular properties and bioactivity score. <http://www.molinspiration.com/cgi-bin/properties>. Accessed 2 Aug 2018.
48. Johannes, T. W. et al. Deciphering the late biosynthetic steps of antimalarial compound FR-900098. *Chem. Biol.* **17**, 57–64 (2010).
49. Richard, S. B. et al. Kinetic analysis of *Escherichia coli* 2-C-methyl-D-erythritol-4-phosphate cytidyltransferase, wild type and mutants, reveals roles of active site amino acids. *Biochemistry* **43**, 12189–12197 (2004).
50. Blodgett, J. A. V. et al. Unusual transformations in the biosynthesis of the antibiotic phosphinothricin tripeptide. *Nat. Chem. Biol.* **3**, 480–485 (2007).
51. Morrison, M. J. & Imperiali, B. The renaissance of bacillosamine and its derivatives: pathway characterization and implications in pathogenicity. *Biochemistry* **53**, 624–638 (2014).
52. D'Souza, K., Kim, Y. J., Balla, T. & Epan, R. M. Distinct properties of the two isoforms of CDP-diacylglycerol synthase. *Biochemistry* **53**, 7358–7367 (2014).
53. Gibellini, F. & Smith, T. K. The Kennedy pathway-de novo synthesis of phosphatidylethanolamine and phosphatidylcholine. *IUBMB Life* **62**, 414–428 (2010).
54. Finn, R. D., Clements, J. & Eddy, S. R. HMMER web server: interactive sequence similarity searching. *Nucleic Acids Res.* **39**, W29–W37 (2011).
55. Finn, R. D. et al. The Pfam protein families database: towards a more sustainable future. *Nucleic Acids Res.* **44**, D279–D285 (2016).
56. Pruitt, K. D., Tatusova, T. & Maglott, D. R. NCBI reference sequences (RefSeq): a curated non-redundant sequence database of genomes, transcripts and proteins. *Nucleic Acids Res.* **35**, D61–D65 (2007).
57. Moreno-Hagelsieb, G., Wang, Z., Walsh, S. & ElSherbiny, A. Phylogenomic clustering for selecting non-redundant genomes for comparative genomics. *Bioinformatics* **29**, 947–949 (2013).
58. Sievers, F. et al. Fast, scalable generation of high-quality protein multiple sequence alignments using Clustal Omega. *Mol. Syst. Biol.* **7**, 539 (2011).
59. Yang, J. et al. The I-TASSER Suite: protein structure and function prediction. *Nat. Methods* **12**, 7–8 (2015).
60. The PyMOL Molecular Graphics System v 1.8. (Schrödinger LLC., 2015).
61. Wang, J., Wolf, R. M., Caldwell, J. W., Kollman, P. A. & Case, D. A. Development and testing of a general amber force field. *J. Comput. Chem.* **25**, 1157–1174 (2004).

62. van der Kamp, M. W. *enlighten: Protocols and tools to run (automated) atomistic simulations of enzyme-ligand systems*. <https://github.com/marcvanderkamp/enlighten> (2018). Accessed 6 July 2018.
63. Roe, D. R. & Cheatham, T. E. PTRAJ and CPPTRAJ: software for processing and analysis of molecular dynamics trajectory data. *J. Chem. Theory Comput.* **9**, 3084–3095 (2013).
64. Wilkins, M. R. et al. Protein identification and analysis tools in the ExPASy server. *Methods Mol. Biol.* **112**, 531–552 (1999).
65. Bradford, M. M. A rapid and sensitive method for the quantitation of microgram quantities of protein utilizing the principle of protein–dye binding. *Anal. Biochem.* **72**, 248–254 (1976).
66. Huitema, C. & Horsman, G. P. Analyzing enzyme kinetic data using the powerful statistical capabilities of R. Preprint at <http://biorxiv.org/content/10.1101/316588v1> (2018).
67. McCoy, A. J. et al. Phaser crystallographic software. *J. Appl. Crystallogr.* **40**, 658–674 (2007).
68. Adams, P. D. et al. PHENIX: building new software for automated crystallographic structure determination. *Acta Crystallogr. D* **58**, 1948–1954 (2002).
69. Emsley, P. & Cowtan, K. Coot: model-building tools for molecular graphics. *Acta Crystallogr. D* **60**, 2126–2132 (2004).

Acknowledgements

We thank Dmitri Goussev and Lana Hiscock (Laurier) for NMR assistance, Masoud Jelokhani-Niaraki and Robin Slawson (Laurier) for equipment access, and Stefano Serapian and Reynier Suardiaz Del Rio (Bristol) for insightful discussions. This work was supported by NSERC, Wilfrid Laurier University, a GlycoNet Catalyst Grant, and a Royal Society of Chemistry Researcher Mobility Grant. We thank the Advanced Computing Research Centre of the University of Bristol (www.bristol.ac.uk/acrc) for computing facilities, and synchrotron data collection facilities of the Advanced Photon Source beamline 17-ID and Canadian Light Source beamline 08-ID-1. M.W.V.d.K. is a BBSRC David Phillips Fellow (BB/M026280/1). K.R., A.P., and D.W. are recipients of a William Nikolaus Martin Scholarship, Ontario Graduate Scholarship and China Scholarship Council funding, respectively.

Author contributions

G.P.H. conceived the project; M.P. and G.M.-H. designed, performed, and analyzed bioinformatic characterization of genomic distances; K.R., K.B., J.K., E.S., A.P., D.W. and

R.S. performed cloning, protein production and purification, biochemical analysis, and enzyme reactions; G.P.H. performed sequence alignments; K.R. performed structural characterization of enzyme products; K.R., K.B. and G.P.H. analyzed enzyme kinetic data; C.B. and J.T.W. performed and analyzed RT-PCR; J.W. performed cloning, purification, and protein crystallization; J.W. and M.D.S. performed protein structure determination; G.P.H. and M.W.V.d.K. designed, performed and analyzed MD simulations; G.P.H. wrote the manuscript with input from all co-authors.

Additional information

Supplementary Information accompanies this paper at <https://doi.org/10.1038/s41467-019-11627-6>.

Competing interests: The authors declare no competing interests.

Reprints and permission information is available online at <http://npg.nature.com/reprintsandpermissions/>

Peer Review Information: *Nature Communications* thanks the anonymous reviewer(s) for their contribution to the peer review of this work.

Publisher's note: Springer Nature remains neutral with regard to jurisdictional claims in published maps and institutional affiliations.



Open Access This article is licensed under a Creative Commons Attribution 4.0 International License, which permits use, sharing, adaptation, distribution and reproduction in any medium or format, as long as you give appropriate credit to the original author(s) and the source, provide a link to the Creative Commons license, and indicate if changes were made. The images or other third party material in this article are included in the article's Creative Commons license, unless indicated otherwise in a credit line to the material. If material is not included in the article's Creative Commons license and your intended use is not permitted by statutory regulation or exceeds the permitted use, you will need to obtain permission directly from the copyright holder. To view a copy of this license, visit <http://creativecommons.org/licenses/by/4.0/>.

© The Author(s) 2019